Valley polarization control in WSe₂ monolayer by a single-cycle laser pulse

Arqum Hashmi [1], Shunsuke Yamada,[2] Atsushi Yamada,[2] Kazuhiro Yabana,[2] and Tomohito Otobe [1,*]

[1]*Kansai Photon Science Institute, National Institutes for Quantum Science and Technology (QST), Kyoto 619-0215, Japan*
[2]*Center for Computational Sciences, University of Tsukuba, Tsukuba 305-8577, Japan*

The valley degree of freedom in two-dimensional materials provides an opportunity to extend the functionalities of valleytronic devices. Very short valley lifetimes demand the ultrafast control of valley pseudospin. Here we theoretically demonstrate the control of valley pseudospin in WSe₂ monolayer by a single-cycle linearly polarized laser pulse. We use the asymmetric electric field controlled by the carrier-envelope phase (CEP) to make the valley polarization between K and K' point in the Brillouin zone (BZ). Time-dependent density functional theory with spin-orbit interaction reveals that no valley asymmetry and its CEP dependence is observed within the linear-optical limit. In the nonlinear-optical regime, a linearly polarized pulse induces a high degree of valley polarization and this polarization is robust against the field strength. Valley polarization strongly depends and oscillates as a function of CEP. The carrier density distribution forms nodes as the laser intensity increases, our results indicate that the position of the carrier density in the BZ can be controlled by the laser intensity. From the analysis by the massive Dirac Hamiltonian model, the nodes of the carrier density can be attributed to the Landau-Zener-Stückelberg interference of wave packets of the electron wave function.

I. INTRODUCTION

Mechanical exfoliation of atomically thin layers by scotch tape from van der Waals bulk crystals has opened up new opportunities for the design of nanoscale quantum materials [1,2]. Specifically, the realization of monolayer graphene in 2004 [3] has ignited extensive research efforts on two-dimensional (2D) layered materials. 2D materials exhibit unique mechanical, optical, and electronic properties compared to their bulk counterparts [4]. Owing to their extraordinary physical properties, the study of 2D monolayers has now been established as an emerging field. For instance, one can find numerous reports on graphene [5], silicene [6], transition metal dichalcogenides (TMDC) [7], and phosphorene [8]. 2D materials have a wide range of applications in the field of electronics and an evolving field of optoelectronics. They feature strong light-matter interaction [4], ultrafast broadband optical response [9], and large optical nonlinearity [10], thus they have a great potential for optoelectronic applications such as photodetectors, tunneling, and imaging devices [2,4,11].

2D materials are classified as magnetic and nonmagnetic semiconductors, topological insulators, metals, and half-metals. Within a wide class of 2D materials family, materials with broken inversion symmetry, such as TMDC monolayers, have received recent attention [12]. The lack of inversion symmetry in TMDC monolayer induces a novel Zeeman type spin splitting which results in two degenerate yet inequivalent valleys in the band structure [13–16]. Valleys are local minima that correspond to different crystal momenta in the reciprocal space. Spin-orbit coupling (SOC) lifts the spin degeneracy in both valleys and the opposite spin angular momenta appear in two valleys owing to the time-reversal symmetry. Thus, the spin-valley locking and the interplay of two inequivalent valleys give rise to valley-dependent optical selection rules [17]. Manipulation of valley pseudospin thus becomes a central theme in the field of valleytronics. Several methods have been proposed to achieve transient valley polarization such as optical excitations [18–20], by applying an external magnetic field and magnetic proximity effect induced by the substrate [21–23]. However, due to the several practical limitations and very short valley lifetimes 10^3–10^6 fs [24], ultrafast control of valley selection on femtosecond timescales is in urgent need.

Experimental demonstration of intense terahertz pulse driven subcycle control of valley dynamics has opened a way to manipulate the valley pseudospin that is switchable within a few fs [25]. Moreover, some theoretical works have also shown the ultrafast control of valley excitation on a fs timescale [26–31]. Recently, valley polarization using few-cycle linearly polarized pulses with the controlled carrier-envelope phase (CEP) has also been proposed by using the density matrix approach [32].

In this work we investigate the linearly polarized single-cycle laser pulse control of valley pseudospin in WSe₂ monolayer employing real-time time-dependent density functional theory (RT-TDDFT). The use of linearly polarized pulses to induce valley polarization differentiate the present study from the previous works where circularly polarized light is used to induce population imbalance between two valleys. Second, the RT-TDDFT can describe electron dynamics under intense laser field without any empirical parameters [33]. We have developed the program for the electron and

*Corresponding author: otobe.tomohito@qst.go.jp

electromagnetic field dynamics, open-source package Scalable *Ab initio* Light-Matter simulator for Optics and Nanoscience (SALMON) [34,35], which employs the RT-TDDFT. We have implemented the SOC with noncollinear local spin density [36–38] to the SALMON version 2.0 to describe the spin-dependent electron dynamics.

Laser intensity and carrier-envelope phase (CEP) dependence of the valley polarization is studied. A linearly polarized single-cycle pulse induces a high degree of valley polarization. Moreover, the valley polarization is robust against the field strength although it oscillates as a function of CEP. We found the distinct node formation of carrier density in the Bloch phase space induced by the quantum interference at strong fields ($\geqslant 10^{11}$ W/cm^2). Our results demonstrate the single optical cycle control of valley pseudospin by linear polarized laser pulses.

II. THEORETICAL FORMALISM

A. RT-TDDFT

We use the 2D approximation method that describes the electron dynamics and light propagation in extremely thin layers at normal incidence [39,40]. Here we briefly describe the theoretical formalism for this method.

The polarization and propagation directions for light pulses are taken along the x axis and z axis, respectively. Also, we assume that the thin layer is in the xy plane. We consider only the x component of vector fields and omit the label "x." By using the Maxwell equations we can describe the propagation of macroscopic electromagnetic fields in the form of the vector potential $A(z, t)$ as

$$\frac{1}{c^2}\frac{\partial^2 A(z,t)}{\partial t^2} - \frac{\partial^2 A(z,t)}{\partial z^2} = \frac{4\pi}{c}J(z,t), \quad (1)$$

where $J(z, t)$ is the macroscopic current density in a thin layer. For an atomic monolayer material, the macroscopic electric current density in Eq. (1) can be expressed as

$$J(z,t) \approx \delta(z)J_{2D}(t), \quad (2)$$

where $J_{2D}(t)$ is 2D current density of the monolayer. We deal with it as a boundary value problem where reflected (transmitted) fields can be determined by the connection conditions at $z = 0$. From Eq. (2) we obtain the continuity equation of $A(z, t)$ at $z = 0$ as follows:

$$A(z = 0, t) = A^{(t)}(t) = A^{(i)}(t) + A^{(r)}(t), \quad (3)$$

where $A^{(i)}$, $A^{(r)}$, and $A^{(t)}$ are the incident, reflected, and transmitted fields, respectively. From the Maxwell equation (1) and Eq. (2) we get the basic equation of the 2D approximation method,

$$\frac{dA^{(t)}}{dt} = \frac{dA^{(i)}}{dt} + 2\pi J_{2D}[A^{(t)}](t). \quad (4)$$

Here $J_{2D}[A^{(t)}](t)$ is the 2D current density that is determined by the vector potential at $z = 0$ and it is equal to $A^{(t)}(t)$.

By using the velocity gauge [41], the time-dependent Kohn-Sham (TDKS) equation using Bloch orbitals $u_{b,\mathbf{k}}(\mathbf{r}, t)$, which is a two-component spinor with b being the band index and k the 2D crystal momentum of the thin layer, is

described as

$$i\hbar\frac{\partial}{\partial t}u_{b,\mathbf{k}}(\mathbf{r},t) = \left[\frac{1}{2m}\left(-i\hbar\nabla + \hbar\mathbf{k} + \frac{e}{c}\mathbf{A}^{(t)}(t)\right)^2 \right.$$
$$\left. - e\varphi(\mathbf{r},t) + \hat{v}_{NL}^{\mathbf{k}+\frac{e}{\hbar c}\mathbf{A}^{(t)}(t)} + v_{xc}(\mathbf{r},t)\right]u_{b,\mathbf{k}}(\mathbf{r},t),$$
$$(5)$$

where the scalar potential $\varphi(\mathbf{r}, t)$ includes the Hartree potential from the electrons and the local part of the ionic pseudopotentials and we have defined $v_{NL}^{\mathbf{k}} \equiv e^{-i\mathbf{k}\cdot\mathbf{r}}\hat{v}_{NL}e^{i\mathbf{k}\cdot\mathbf{r}}$, where $\hat{v}_{NL}$ is the nonlocal part of the ionic pseudopotential. $v_{xc}(r, t)$ is the exchange-correlation potential. The SOC is incorporated through the j-dependent nonlocal potential $\hat{v}_{NL}$ [38]. The Bloch orbitals $u_{b,\mathbf{k}}(\mathbf{r}, t)$ are defined in a box containing the unit cell of the 2D thin layer sandwiched by vacuum regions. The 2D current density $J_{2D}[A^{(t)}](t)$ in Eq. (4) is derived from the Bloch orbitals as follows:

$$\mathbf{J}_{2D}(t) = -\frac{e}{m}\int dz \int_\Omega \frac{dx\,dy}{\Omega}\sum_{b,\mathbf{k}}^{occ} u_{b,\mathbf{k}}^\dagger(\mathbf{r},t)$$
$$\times \left\{-i\hbar\nabla + \hbar\mathbf{k} + \frac{e}{c}\mathbf{A}^{(t)}(t) + \frac{m}{i\hbar}\left[\mathbf{r}, \hat{v}_{NL}^{\mathbf{k}+\frac{e}{\hbar c}\mathbf{A}^{(t)}(t)}\right]\right\}$$
$$\times u_{b,\mathbf{k}}(\mathbf{r},t), \quad (6)$$

where Ω is the area of the unit cell and the sum is taken over the occupied orbitals in the ground state. In the 2D approximation method, coupled Eqs. (4) and (5) are simultaneously solved in real time.

The excited electron population is defined as

$$\rho_{\boldsymbol{k}}(t) = \sum_{c,v}\left|\int_\Omega d^3r\, u_{v,\mathbf{k}}^*(\mathbf{r},t)\, u_{c,\mathbf{k}+\frac{e}{\hbar c}\hat{x}A^{(t)}(t)}^{GS}(\mathbf{r})\right|^2, \quad (7)$$

where v and c are the indices for the valence and conduction bands, respectively, and $u_{b,\mathbf{k}}^{GS}(\mathbf{r}) = u_{b,\mathbf{k}}(\mathbf{r}, t = 0)$ is the Bloch orbital in the ground state.

RT-TDDFT calculations are performed using SALMON version 2.0. The lattice constant of WSe$_2$ monolayer is set to $a = b = 3.32$ Å. The adiabatic local density approximation with Perdew-Zunger functional [42] is used for the exchange correlation. A slab approximation is used for the z axis with the distance of 20 Å between the atomic monolayers. The dynamics of the 24 valence electrons are treated explicitly while the effects of the core electrons are considered through norm-conserving pseudopotentials from the OpenMX library [43]. The spatial grid sizes and k points are optimized according to the converge results. The determined parameter of the grid size is 0.21 Å while the optimized k mesh is 15×15 in the 2D Brillouin zone (BZ).

B. Two-band model

In order to understand the physical mechanism behind the RT-TDDFT results, we perform model calculations using a minimal band model [15,44,45]. The model Hamiltonian including the second order coupling for the low energy physics

around K or K' point is described as below:

$$H^\tau[k] = \begin{pmatrix} \frac{\Delta}{2} & \tau a \tilde{t} k \\ \tau a \tilde{t} k & -\frac{\Delta}{2} \end{pmatrix} + a^2 k^2 \begin{pmatrix} \gamma_1 & \gamma_3 \\ \gamma_3 & \gamma_2 \end{pmatrix} + \begin{pmatrix} 0 & 0 \\ 0 & \tau s \lambda \end{pmatrix},$$
(8)

where $\tau = +1(-1)$ corresponds to the K (K') point, a is the lattice constant, Δ is the band gap, $\tilde{t}$ is the hopping parameter, λ is the spin-orbit splitting of the valence band, and k is relative to τK. Here we consider only the electron motion along the x axis and omit the y direction ($k_y = 0$). The parameters γ_1 and γ_2 represent the breaking of the electron-hole symmetry. The parameter γ_3 is responsible for the band asymmetry. These parameters are determined by fitting the calculated band structure by SALMON. The first and second terms are the massive Dirac Hamiltonian and its second order correction term, respectively. The third term is the spin-orbit coupling Hamiltonian and $s = \pm 1$ is the spin index.

By diagonalizing the Hamiltonian we have the conduction and valence wave functions at the ground state:

$$\phi_{ck}^\tau = \begin{pmatrix} \sqrt{\frac{\Omega_k^\tau + \alpha_k^\tau}{2\Omega_k^\tau}} \\ s_k^\tau \sqrt{\frac{\Omega_k^\tau - \alpha_k^\tau}{2\Omega_k^\tau}} \end{pmatrix}, \quad \phi_{vk}^\tau = \begin{pmatrix} \sqrt{\frac{\Omega_k^\tau - \alpha_k^\tau}{2\Omega_k^\tau}} \\ -s_k^\tau \sqrt{\frac{\Omega_k^\tau + \alpha_k^\tau}{2\Omega_k^\tau}} \end{pmatrix}, \quad (9)$$

where $\alpha_k^\tau = (H_{11}^\tau[k] - H_{22}^\tau[k])/2$ and $\Omega_k^\tau = \sqrt{(\alpha_k^\tau)^2 + (H_{12}^\tau[k])^2}$. Here $s_k^\tau = \mathrm{sgn}\, H_{12}^\tau[k]$ is the sign factor of the off-diagonal element.

The electron dynamics in the presence of the electric field $E(t)$ is described by

$$i\hbar \frac{d}{dt} \psi_k^\tau(t) = H^\tau\left[k + \frac{e}{\hbar c} A(t)\right] \psi_k^\tau(t),$$
(10)

where $\psi_k^\tau(t) = (\psi_1^{\tau k}(t), \psi_2^{\tau k}(t))^T$ is the time-dependent wave function and $A(t)$ is the vector potential [it satisfies $E(t) = -(1/c)dA(t)/dt$]. The initial value of the wave function is taken as follows:

$$\psi_k^\tau(t=0) = \phi_{vk}^\tau.$$
(11)

The excitation probability from the valence band to the conduction band is written as

$$P^\tau(t) = \frac{1}{N_k} \sum_k |\langle \phi_{ck}^\tau | \psi_k^\tau(t) \rangle|^2,$$
(12)

where the sum is taken over a certain region of the k-point sampling around $k = 0$. N_k is the number of the sampling points.

To get an intuitive understanding for the transition, we describe below an approximate evaluation of Eq. (12) using the Landau-Zener theory ignoring the second and third terms in the Hamiltonian of Eq. (8). We note that the Landau-Zener theory is a semiclassical approximation and can be justified when the applied electric field is sufficiently strong. The valence and conduction eigenenergies are given by

$$\varepsilon_{ck} = +\Omega(k), \quad \varepsilon_{vk} = -\Omega(k), \quad \Omega(k) \equiv \sqrt{\frac{\Delta^2}{4} + a^2 \tilde{t}^2 k^2}.$$
(13)

In this paper we utilize a single-cycle pulse for all the calculations. In such cases we can assume that the Landau-Zener transitions occur twice at times t_1 and t_2 ($t_2 > t_1$) for each k

point, at which the vector potential crosses k as follows:

$$k + \frac{e}{\hbar c} A(t_{1,2}) = 0.$$
(14)

The tunneling probability at t_1 and t_2 may be written as P_{LZ} and $1 - P_{LZ}$, respectively, where

$$P_{LZ} = \exp\left(-2\pi \frac{\Delta^2}{4\hbar v}\right), \quad v = \frac{2e}{\hbar}|E(t_1)| a \tilde{t}. \quad (15)$$

By considering the phase factor due to the adiabatic time evolution, we have

$$P(t) \sim 4 P_{LZ}(1 - P_{LZ}) \sin^2\left[\int_{t_1}^{t_2} dt\, \Omega\left(k + \frac{e}{\hbar c} A(t)\right)\right]. \quad (16)$$

The interference that originates from two transitions at t_1 and t_2 is known as the Landau-Zener-Stückelberg interference. The cancellation condition by the Landau-Zener-Stückelberg interference is given as

$$\int_{t_1}^{t_2} dt\, \Omega\left(k + \frac{e}{\hbar c} A(t)\right) = 0.$$
(17)

Although the Landau-Zener-Stückelberg theory provides a simple and intuitive understanding for excitation processes, we should note that it provides results of quantitative accuracy for a limited parameter region.

III. RESULTS AND DISCUSSION

Figure 1(a) shows the monolayer of WSe₂ along with the first BZ. WSe₂ is a layered structure where W atoms are sandwiched between the top and bottom Se layers in a hexagonal lattice. The six corners of hexagonal BZ contain two inequivalent high symmetry K and K' points at the edges owing to the honeycomb crystal structure. The real space armchair direction of WSe₂ belongs to Γ-M while zigzag corresponds to Γ-K in reciprocal space. Figure 1(b) shows the dispersion of the bands [conduction band minimum (CBM) - valence band maximum (VBM)] as a function of the wave vector k in the whole BZ. The band contour at K (K') points is a triangle and this so-called trigonal warping indicates the anisotropic carrier distributions in the WSe₂ monolayer. The electronic band structure of the WSe₂ is shown in Fig. 1(c). WSe₂ has a direct band gap of 1.25 eV at K (K') and, due to the lack of inversion symmetry, all bands are split by the intrinsic SOC except at the time-reversal invariant Γ and M point. Thus, owing to time-reversal symmetry and strong SOC, the top of the valence band of WSe₂ is spin up (spin down) in the K (K') valley. The energy degenerate valleys have a large VBM spin splitting of ~0.45 eV that agrees well with previous studies [14–16].

Long pulses containing several optical cycles resemble a continuous wave where maxima of electric field concurrence with the zero of the vector potential. In contrast, for ultrashort pulses containing a few optical cycles, the condition [maxima of $E(t) = 0$ of $A(t)$] can be controlled by CEP (φ). φ is the relative phase of the pulse envelope and the oscillating electric field which plays a significant role in the pulse waveform for ultrashort laser pulses. Thus, we are taking advantage of φ to manipulate the valley polarization by using a laser pulse of a single optical cycle. To explore the φ dependence on
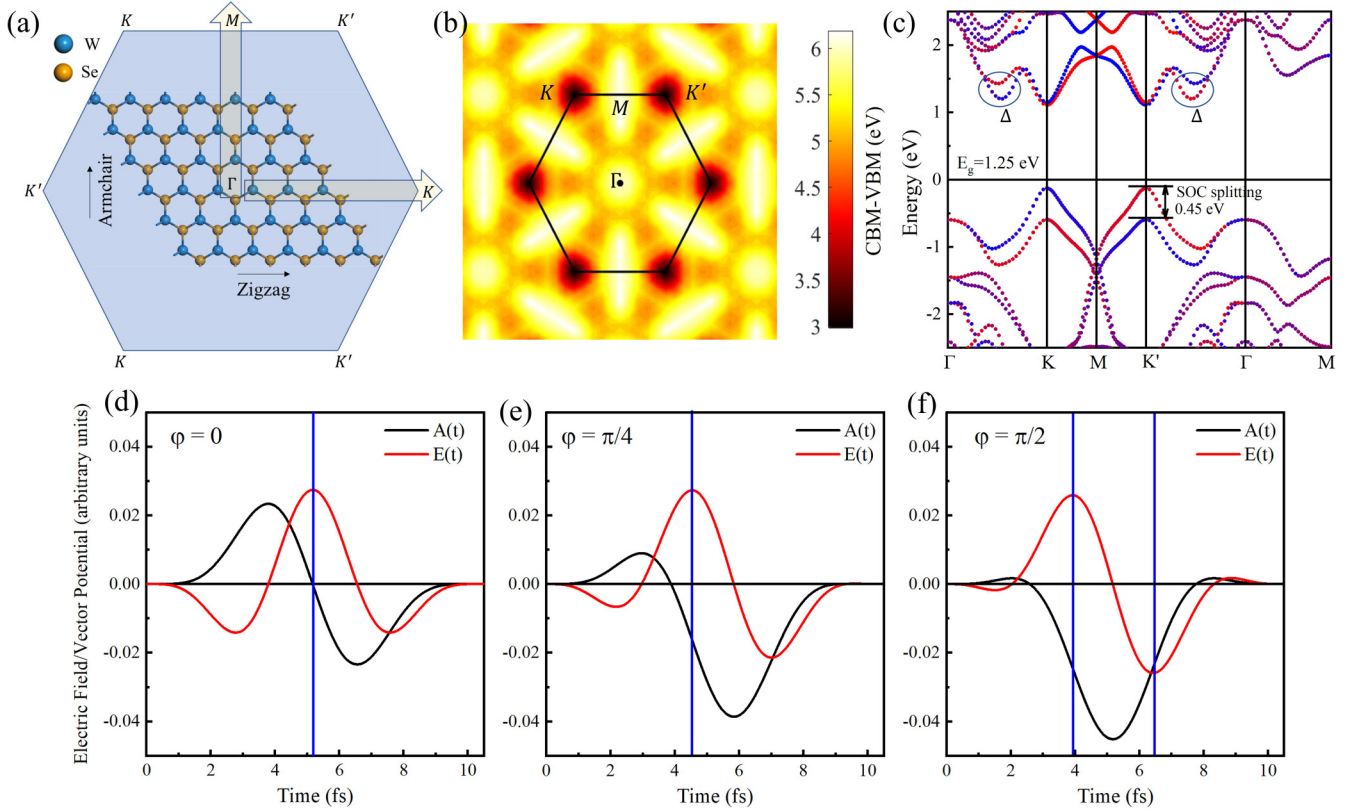
FIG. 1. (a) WSe$_2$ monolayer along with the first BZ. The relevant polarization directions, armchair (Γ-M in reciprocal space), and zigzag (Γ-K) are labeled by arrows. (b) 2D WSe$_2$ energy map of (CBM-VBM) as a function of the wave vector k in the hexagonal BZ, and (c) WSe$_2$ band structure along high symmetry directions. The red and blue dots correspond to $S_z = \uparrow$ and $S_z = \downarrow$ respectively. Electric field and vector potential of single-cycle 10 fs long linearly polarized laser dependence at various CEP: (d) $\varphi = 0$, (e) $\varphi = \frac{\pi}{4}$, and (f) $\varphi = \frac{\pi}{2}$.

valley pseudospin, we apply linearly polarized pulses parallel to armchair (Γ-M) and zigzag (Γ-K) directions. We use the vector potential of the following waveform:

$$A^{(i)}(t) = -\frac{cE_{\max}}{\omega} f(t) \cos\left\{\omega\left(t - \frac{T_P}{2}\right) + \varphi\right\}, \qquad (18)$$

where ω is the average frequency, $E_{\max}$ is the maximum amplitude of the electric field, φ is CEP, and T_P is the pulse duration. The pulse envelope function is of $\cos^4$ shape for the vector potential given as

$$f(t) = \begin{cases} \cos^4\left(\pi \frac{t - T_P/2}{T_P}\right) & 0 \leqslant t \leqslant T_P, \\ 0 & \text{otherwise.} \end{cases} \qquad (19)$$

We use the frequency of 0.4 eV, the pulse length is set to $T_P = 10$ fs and the total computation time is twice the pulse length, and the time step size is set to 5×10^{-4} fs. Figures 1(d)–1(f) show the electric field and vector potential dependence on φ. At $\varphi = 0$, the peak of the electric field coincides with the zero of vector potential. For $\varphi = \frac{\pi}{4}$, vector potential has a nonzero value at the peak of the pulse envelope while at $\varphi = \frac{\pi}{2}$ the electric field has positive and negative peaks with the nonzero value of vector potential.

We start from the field polarized along the Γ-M direction. The band contour along with the electronic band structure [see Figs. 1(b) and 1(c)] displays no asymmetry in Γ-M direction.

Thus, we do not expect valley polarization for the field polarized along the Γ-M direction. Note that for confirmation, valley population at the end of a single cycle is checked at different φ, the valley population is found to be indifferent at both K and K' valley (not shown here). Hence, valley polarization does not exist for the field polarized along Γ-M because of the lattice symmetry in that direction. On the other hand, owing to trigonal wrapping, the polarization parallel to Γ-K experiences different band curvature with respect to K and K' point. Hence, the field polarized along the Γ-K may experience strong asymmetries that can lead to the possibility of generating valley polarization. Therefore, from now on we will focus on the Γ-K direction.

Figures 2(a)–2(c) shows the excitation energy for various laser intensities at $\varphi = 0$, $\frac{\pi}{4}$, and $\frac{\pi}{2}$, respectively calculated by the RT-TDDFT. Excitation energy is defined as the difference of the energy density integrated over the unit cell that include three atoms at time t and that in the ground state. For weak intensity (10^9 and 10^{10} W/cm^2), the excitation energy is pronounced during the irradiation of the pulsed electric field and turns out to be zero as soon as the pulse ends because the electronic state goes back to its ground state. On the other hand, the excitation energy at the intense field ($>10^{10}$ W/cm^2) is substantially large and does not vanish even after the pulse ends. Excitation energy has a more interesting dependence on the φ that is independent of the laser intensity. For $\varphi = 0$ and
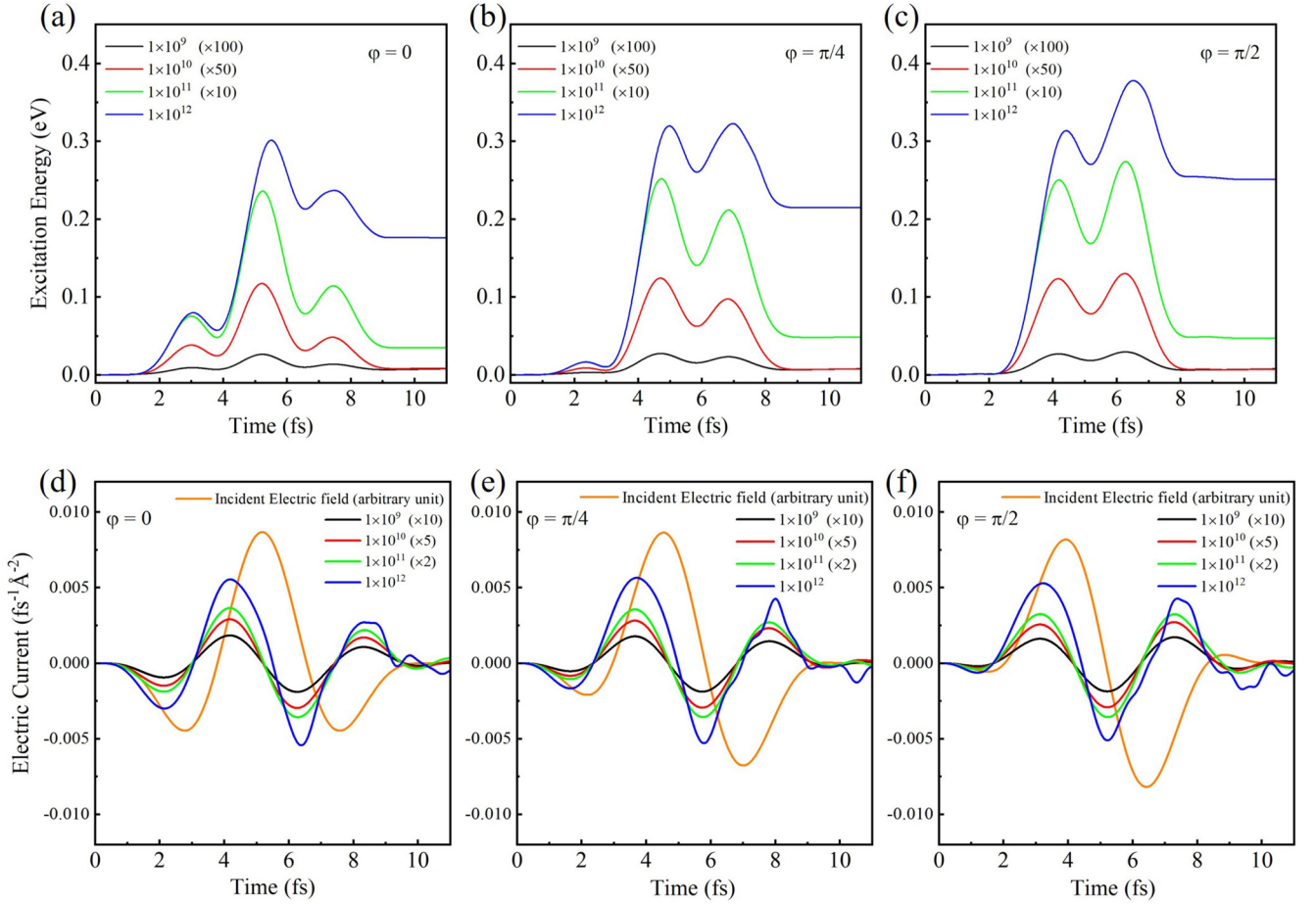
FIG. 2. Temporal development of excitation energies for various intensities at CEP: (a) $\varphi = 0$, (b) $\varphi = \frac{\pi}{4}$, and (c) $\varphi = \frac{\pi}{2}$. Applied pulsed electric field and Induced electric current density as a function of time at CEP: (d) $\varphi = 0$, (e) $\varphi = \frac{\pi}{4}$, and (f) $\varphi = \frac{\pi}{2}$. For a clear comparison, the results of weak pulses are rescaled up by multiplying with numerous factors.

$\frac{\pi}{4}$ the electric field has one maxima that is present in the first half-cycle of the pulse, thus the excitation energy is dominant in the first half and reduces in the other half-cycle. In contrast, the electric field at $\varphi = \frac{\pi}{2}$ has two field maxima (positive and negative) and the excitation energy is even higher in the second half than the first half-cycle. In addition, at the given intensity the total excitation energy has the order of $\varphi = \frac{\pi}{2} > \varphi = \frac{\pi}{4} > \varphi = 0$.

Before going to the detailed discussion on valley polarization, the time profile of the incident electric field and the induced electric current density by RT-TDDFT at multiple φ is shown in Figs. 2(d)–2(f). The current density depends on the electric field amplitude as well as on the φ. But regardless of the field amplitude and φ, the current is not in phase with the incident electric field representing the typical semiconducting optical response of WSe$_2$ monolayer. The current density at the weak electric field ($I = 10^9$ W/cm^2) indicates the linear optical response due to a similar time profile to the pulsed electric field. As the field amplitude increases, the current starts to depart from the linear response and the distortion in current density becomes very visible at the intensity $I = 10^{12}$ W/cm^2, an indication of the strong nonlinear response of electrons. The behavior of the excitation energy and current density indicates that valley asymmetry will have a strong dependence on the intensity and φ.

We further investigate the distribution of k-resolved electron populations of the conduction band. Valley population calculated by the RT-TDDFT method has been shown in Fig. 3 at various intensities and φ at the end of the pulse using Eq. (7). First, we discuss the effect of intensity on the valley population. Starting from a very weak intensity of 1×10^9 W/cm^2, we find an equal population at K and K' point, moreover, φ dependence is also not realized in the valley population. Hence, no valley asymmetry is present within the limit of linear optics. As we increase the intensity to 1×10^{10} W/cm^2, the difference in the population at K and K' point starts to arise. Further increase in intensity not only increases the difference in the population at two valleys but also the carrier density starts to shift around K and K' points.

The intensity dependence can be understood in a simple manner, as the laser interacts with the WSe$_2$ monolayer, electrons start to tunnel from VBM to CBM. At weak intensity, the tunneling from VBM to CBM is very weak and it becomes stronger with the increase in intensity. The formation of nodes in carrier density distribution at intense laser fields is observed around K (K') point. Furthermore, the difference in valley population also strongly depends on φ. As we described above, at $\varphi = 0$, vector potential is zero at the maxima of the electric field owing the laser field couple equally to both valleys regardless of the intensity. As the φ is varied, the value
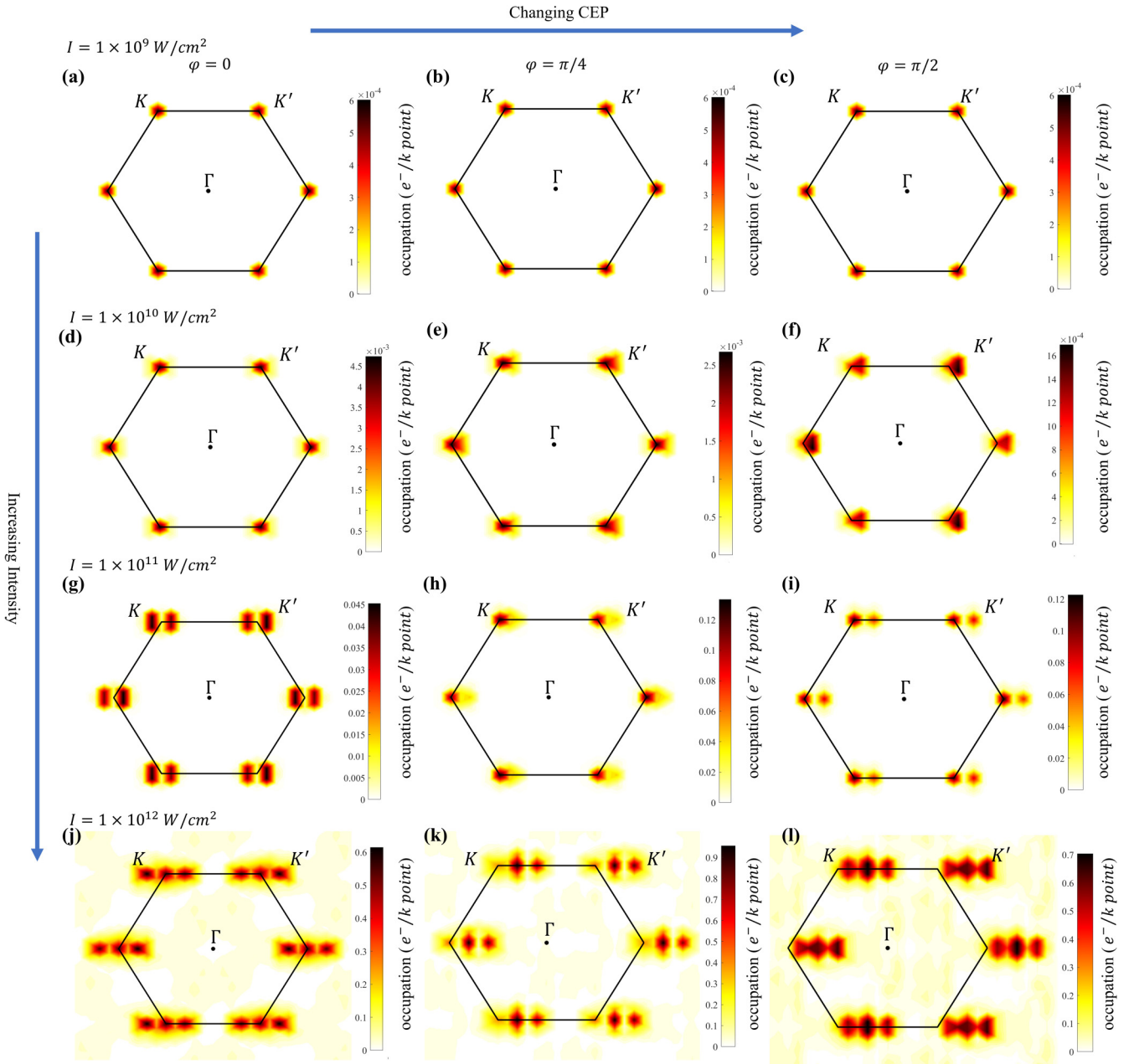
FIG. 3. Distribution of k-resolved electron populations in the first BZ of the conduction band at the end of a single optical cycle pulse. Electron population is summed over the entire conduction band, at various CEP and intensities. Electron population along Γ-K direction at $I = 1 \times 10^9$ W/cm^2 field for CEP: (a) $\varphi = 0$, (b) $\varphi = \frac{\pi}{4}$, and (c) $\varphi = \frac{\pi}{2}$. (d)–(f) The same as (a)–(c) for $I = 1 \times 10^{10}$ W/cm^2, (g)–(i) for $I = 1 \times 10^{11}$ W/cm^2, while (j)–(l) is for $I = 1 \times 10^{12}$ W/cm^2.

of the vector potential at the field peaks changes which control the population difference between two valleys. The results of the k-resolved population reveal that the valley asymmetry by linearly polarized pulses is a nonlinear optical phenomenon.

To explore the valley asymmetry as a function of φ, valley polarization is calculated by the RT-TDDFT, shown in Fig. 4 (a). Valley polarization is defined as

$$V_P = 2 \frac{\rho_{n,K} - \rho_{n,K'}}{\rho_{n,K} + \rho_{n,K'}}, \qquad (20)$$

where $\rho_{n,K} (\rho_{n,K'})$ is obtained by integrating the electron population in a so-called triangle area whose size corresponds to

the same spin area around K (K') point. Note that electron population switches to the opposite valley when the vector potential changes its sign from negative to positive for $\varphi > \pi$. The valley polarization for weakest intensity $I = 1 \times 10^9$ W/cm^2 is zero for all CEP, which confirms the fact that the valley polarization is absent within the linear-optical limit. By increasing the intensity, we enter in the nonlinear regime and the substantial valley polarization is observed for $I = 1 \times 10^{10}$ W/cm^2. The valley polarization increases gradually with φ and reaches its maximum value at $\varphi = \frac{\pi}{2}$, showing a typical sine wave curve. The valley polarization increases more and also inverted its sign with the further increase in
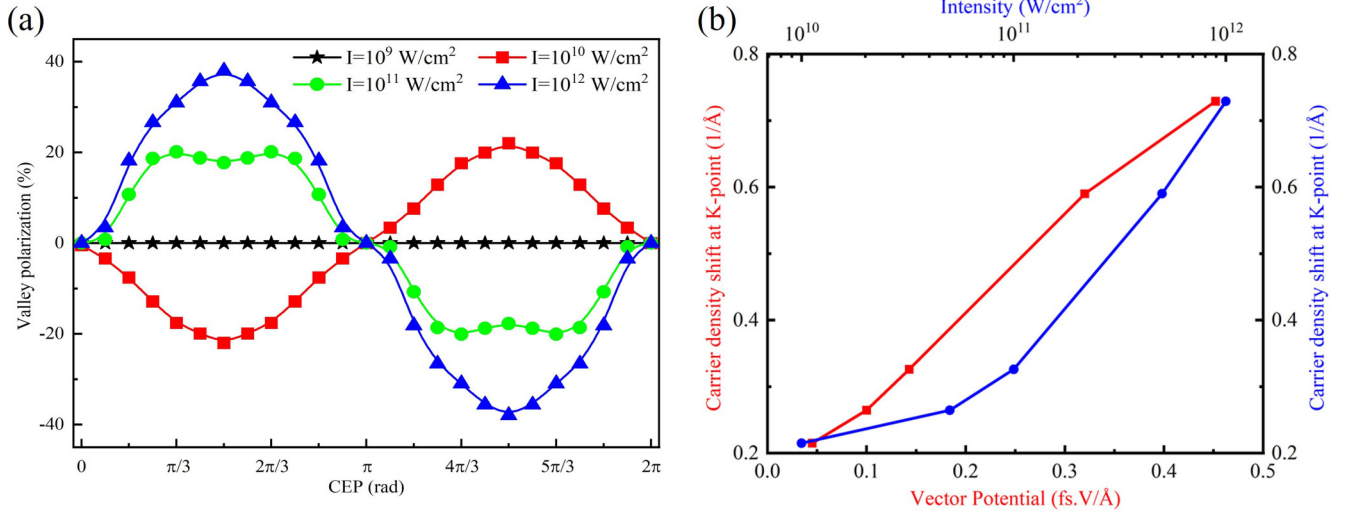
FIG. 4. (a) Valley polarization as a function of CEP at multiple intensities. (b) Shift in the carrier density as a function of the vector potential amplitude and intensity.

intensity. The maximum valley polarization is achieved for the strongest intensity of 1×10^{12} W/cm^2 and the valley polarization is almost twice as compared to 1×10^{10} W/cm^2. Valley polarization is robust against field strength but in all cases oscillate as a function of CEP. Although, the valley polarization is much smaller than the one-photon optical excitation with circularly polarized pulses. Nonetheless, a sinelike curve as shown in Fig. 4(a) indicates that the valley polarization induced by a linearly polarized pulse can be realized experimentally.

As shown in Fig. 3, the carrier density starts to shift around K (K') point and the carrier density distribution starts to form nodes at strong field intensities. This laser intensity dependence indicates that the position of the carrier density in the BZ can be controlled with laser intensity. Figure 4(b) shows the shift in the carrier density as a function of the vector potential amplitude and intensity at $\varphi = \pi/2$. Shift in the carrier density is obtained by calculating the spreading area of excitation from mean position of the carrier density to K point in the BZ. The vector field amplitude has a linear dependence on the shift of carrier density. By increasing the intensity, more nodes in the carrier population start to appear and this may refer to stronger quantum interferences of wave packets. This will be explained in detail in the last section.

To go through the valley polarization details, we have drawn the band resolved charge and spin-decomposed carrier population calculated by the RT-TDDFT. Figure 5(a) shows the temporal evolution of charge and spin-resolved population of intensity 1×10^{10} W/cm^2 at $\varphi = \frac{\pi}{2}$. The main concerned bands involved in this process are CBM-1 and CBM-2 that represent the spin-orbit splitted lower and upper energy conduction band, respectively. Three time steps are chosen at around the first and second maxima of the electric field and at the end of the pulse. CBM-2 has the same spin as VBM thus at 4.0 fs the electrons are excited to CBM-2 at K (K'). One can see that at 7.0 fs, which is the second half of the pulse, more electrons are excited and we note the asymmetry in the population at that point. The excited electron

population becomes small when the laser field ends at 10 fs because most of the electrons go back to their ground state due to very weak intensity. Spin is also confined at K and K' points. The charge and spin-resolved population of intensity 1×10^{11} W/cm^2 is shown in Fig. 5(b) at $\varphi = \frac{\pi}{4}$ (where we find the maximum valley asymmetry). Charge and spin dynamics are the same as found at 1×10^{10} W/cm^2 intensity, nevertheless the excited electrons reside in the CBM-2 even as the pulse ends. At the most intense case of the 1×10^{12} W/cm^2 field, we find highly nonlinear interaction and electrons spread more widely throughout the Brillouin zone as shown in Fig. 5(c). The delta (Δ) points at CBM close to K (K') with opposite spin [see Fig. 1(c)] play an important role at this strong intensity. Δ point acts as an intermediate point which facilitates the intervalley transfer of excited electrons to lower and upper conduction bands. Thus, unlike the other cases, the charge along with the spin is not limited to CBM-2 and multiple conduction bands start to contribute in valley polarization.

The spin polarization of excited charge carriers is shown in Fig. 5(d). Overall the spin polarization ($N_\uparrow - N_\downarrow$) is negligible and independent of intensity and φ, except small spin starts to appear at $I = 1 \times 10^{12}$ W/cm^2. Degree of spin polarization ($N_\uparrow - N_\downarrow$)/($N_\uparrow + N_\downarrow$) follow the same behavior as valley polarization which shows that spin polarization is also an observable along with valley polarization.

The valley polarization results calculated by the two-band model as a function of φ are shown in Fig. 6(a). The two-band model qualitatively reproduces the overall trends of valley polarization with RT-TDDFT results. The origin of the carrier density nodes at higher intensities and the phase change of the valley polarization with respect to intensity can be explained by the two-band model. Based on the massive Dirac model, the phase appearing in the Landau-Zener formula is referred to as Stückelberg phase as described in Eqs. (16) and (17). The recurring Landau-Zener transitions driven by an oscillatory external field produces an excitation density matrix with an opposite sign which causes the interference of the wave
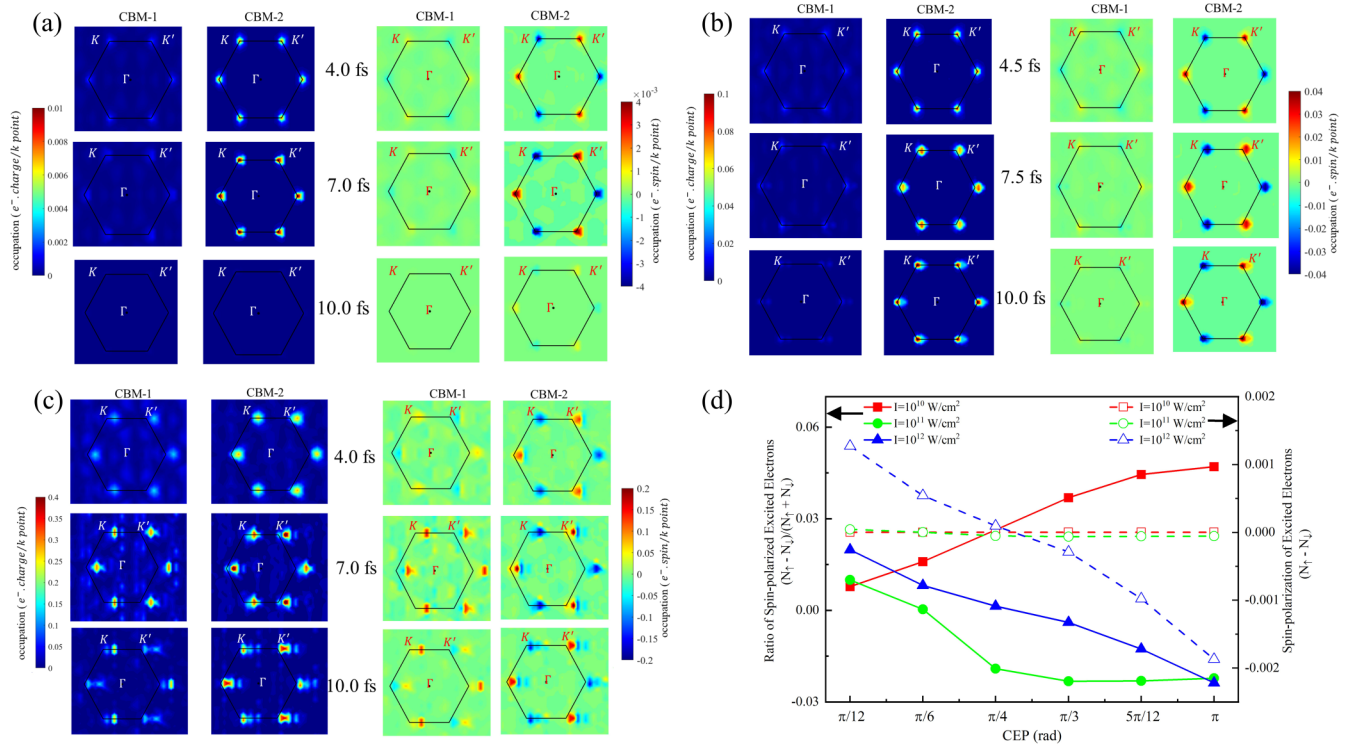
FIG. 5. Charge and spin-decomposed carrier population of concerned conduction bands named as CBM-1 and CBM-2 at different time steps for (a) $I = 1 \times 10^{10}$ W/cm^2, (b) $I = 1 \times 10^{11}$ W/cm^2, and (c) $I = 1 \times 10^{12}$ W/cm^2. (d) Spin polarization of excited charge carriers as a function of CEP.

packets. Thus the carrier density nodes appearing at high intensity may refer to the Stückelberg interference where the excitation probability becomes zero at a certain k.

Figure 6(b) shows the intensity dependence of the valley polarization at $\varphi = \frac{\pi}{2}$. Valley polarization has a very complex behavior regarding the phase change. Thus to find the origin of the phase change, we have shown the excitation probability in Figs. 6(c)–6(e). The excitation probability of $P(K + k) > P(-K + k)$ at 1×10^{10} W/cm^2, as we increase intensity, $P(-K + k)$ starts to increase, and the excitation probability is roughly the same at 8×10^{10} W/cm^2. Further increase in intensity results in $P(K + k) < P(-K + k)$ and this brings the phase change of the valley polarization. Overall, the Stückelberg interference first takes place at the positive k region, and asymmetry is observed at the peak caused by the interference. The peak at the negative k region follows at higher intensities and causes stronger interference of wave packets.

Finally, it is worth commenting that the valley polarization induced by the linearly polarized light mainly depends on the two factors. First, the asymmetry in the band structure plays the main role to generate valley polarization. The band contour displays no asymmetry in the Γ-M direction. Thus, even by varying the CEP, no valley polarization is achieved in this direction. On the other hand, the field polarization parallels to Γ-K experiences different band curvature with respect to K and K' point which results in the valley polarization in WSe$_2$ monolayer. Second, CEP plays a critical role to create valley polarization in Γ-K direction. For $\varphi = 0$, because the vector potential $A(t) = 0$ at the maxima of $E(t)$, we do not observe any asymmetry even if there is a band asymmetry. On the

other hand, for example, at $\varphi = \frac{\pi}{2}$, the vector potential $A(t)$ has a finite negative value at both maxims of $E(t)$, thus a large asymmetry of excitation because the band asymmetry is observed.

IV. CONCLUSION

In conclusion, we investigated the single-cycle pulse control of valley pseudospin in the WSe$_2$ monolayer. The intensity and CEP dependence of the pulsed electric field is varied to investigate the mechanism of valley polarization. Linearly polarized pulse along armchair and zigzag directions are applied.

Valley polarization remains zero within the linear optical limit for both polarization directions. In the nonlinear regime, there is no valley asymmetry and its CEP dependency is realized for the field polarized along the armchair direction while the polarization, which parallels the zigzag direction, experiences strong asymmetries. The valley polarization is small at weak intensities but it increases with the increase in intensity and substantial valley polarization is achieved. The valley polarization is robust against field strength but it strongly depends on the CEP.

We showed that in the strong-field regime the electron dynamics display quantum interference that gives rise to distinct node formation. More importantly, the position of the carrier density is strongly dependent on laser intensity which indicates the possibility to control the electron momentum in BZ. The two-band model indicates that the carrier density nodes appearing at high intensity may refer to the Stückelberg interference.
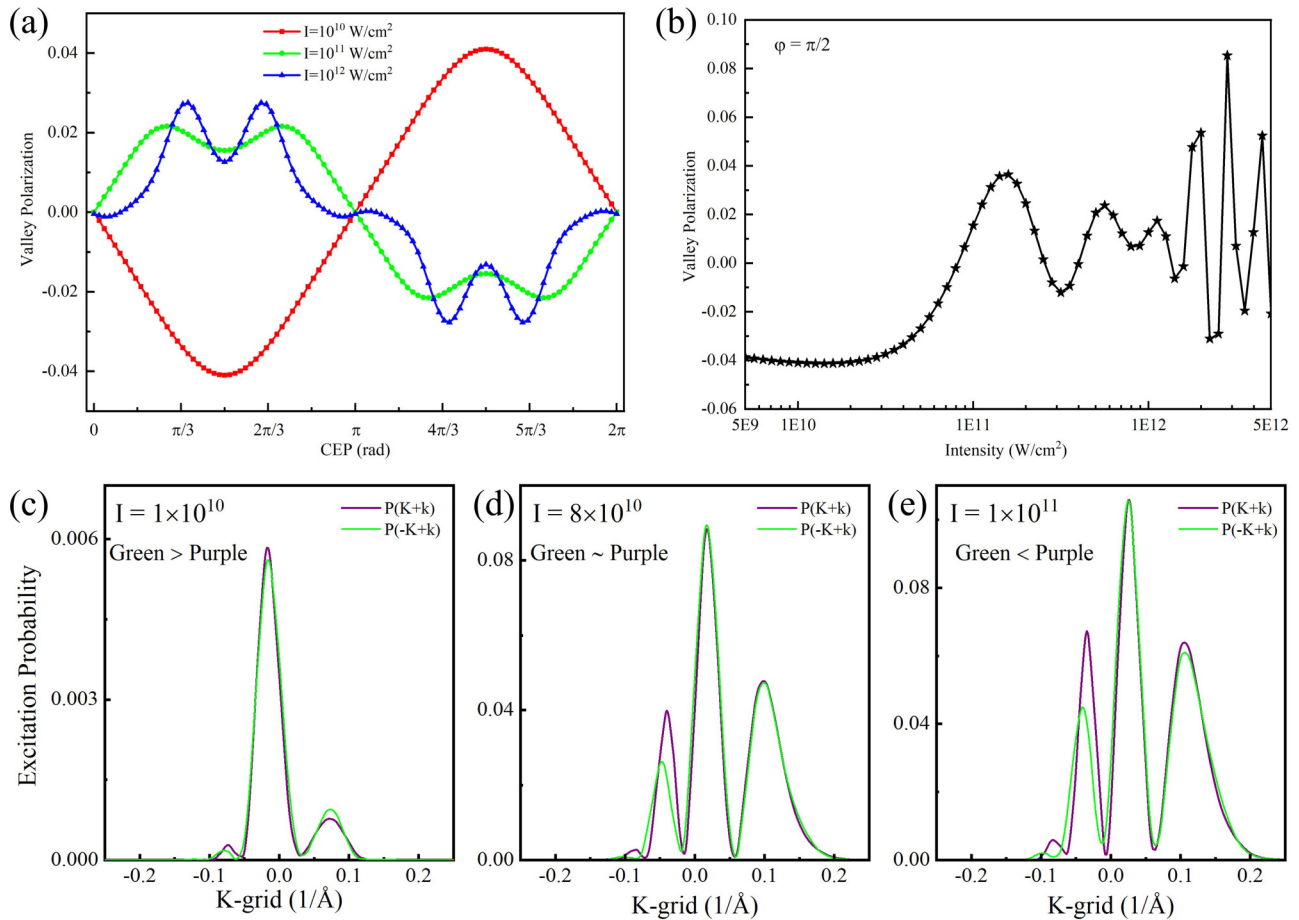
FIG. 6. Massive Dirac Hamiltonian two-band model results. (a) Valley polarization as a function of CEP at multiple intensities. (b) Valley polarization as a function of intensity at $\varphi = \pi/2$. Excitation probabilities at (c) 1×10^{10} W/cm², (d) 8×10^{10} W/cm², and (e) 1×10^{11} W/cm².

Our results provide the opportunity to manipulate the valley pseudospin and optical field control of electron dynamics faster than electron-electron scattering and electron-phonon scattering.

ACKNOWLEDGMENTS

[1] M. Osada and T. Sasaki, Two-dimensional dielectric nanosheets: Novel nanoelectronics from nanocrystal building blocks, Adv. Mater. **24**, 210 (2012).

[2] M. Chhowalla, H. S. Shin, G. Eda, L.-J. Li, K. P. Loh, and H. Zhang, The chemistry of two-dimensional layered transition metal dichalcogenide nanosheets, Nat. Chem. **5**, 263 (2013).

[3] K. S. Novoselov, A. K. Geim, S. V. Morozov, D. Jiang, Y. Zhang, S. V. Dubonos, I. V. Grigorieva, and A. A. Firsov, Electric field effect in atomically thin carbon films, Science **306**, 666 (2004).

[4] S. Kang, D. Lee, J. Kim, A. Capasso, H. S. Kang, J.-W. Park, C.-H. Lee, and G.-H. Lee, 2D semiconducting materials for electronic and optoelectronic applications: potential and challenge, 2D Mater. **7**, 022003 (2020).

[5] K. S. Novoselov, V. I. Falko, L. Colombo, P. R. Gellert, M. G. Schwab, and K. Kim, A roadmap for graphene, Nature (London) **490**, 192 (2012).

[6] L. Tao, E. Cinquanta, D. Chiappe, C. Grazianetti, M. Fanciulli, M. Dubey, A. Molle, and D. Akinwande, Silicene field-effect transistors operating at room temperature, Nat. Nanotechnol. **10**, 227 (2015).

[7] Q. H. Wang, K. Kalantar-Zadeh, A. Kis, J. N. Coleman, and M. S. Strano, Electronics and optoelectronics of two-dimensional transition metal dichalcogenides, Nat. Nanotechnol. **7**, 699 (2012).

[8] F. Xia, H. Wang, and Y. Jia, Rediscovering black phosphorus as an anisotropic layered material for optoelectronics and electronics, Nat. Commun. **5**, 4458 (2014).

[9] T. Tan, X. Jiang, C. Wang, B. Yao, and H. Zhang, 2D material optoelectronics for information functional device applications: Status and challenges, Adv. Sci. **7**, 2000058 (2020).

[10] X. Wen, Z. Gong, and D. Li, Nonlinear optics of two-dimensional transition metal dichalcogenides, InfoMat **1**, 317 (2019).

[11] X. Zhou, X. Hu, J. Yu, S. Liu, Z. Shu, Q. Zhang, H. Li, Y. Ma, H. Xu, and T. Zhai, 2D layered material-based van der Waals heterostructures for optoelectronics, Adv. Funct. Mater. **28**, 1706587 (2018).

[12] J. R. Schaibley, H. Yu, G. Clark, P. Rivera, J. S. Ross, K. L. Seyler, W. Yao, and X. Xu, Valleytronics in 2D materials, Nat. Rev. Mater. **1**, 16055 (2016).

[13] W. Yao, D. Xiao, and Q. Niu, Valley-dependent optoelectronics from inversion symmetry breaking, Phys. Rev. B **77**, 235406 (2008).

[14] Z. Y. Zhu, Y. C. Cheng, and U. Schwingenschlögl, Giant spin-orbit-induced spin splitting in two-dimensional transition-metal dichalcogenide semiconductors, Phys. Rev. B **84**, 153402 (2011).

[15] D. Xiao, G.-B. Liu, W. Feng, X. Xu, and W. Yao, Coupled Spin and Valley Physics in Monolayers of MoS$_2$ and Other Group-VI Dichalcogenides, Phys. Rev. Lett. **108**, 196802 (2012).

[16] H. Yuan, M. S. Bahramy, K. Morimoto, S. Wu, K. Nomura, B.-J. Yang, H. Shimotani, R. Suzuki, M. Toh, C. Kloc *et al.*, Zeeman-type spin splitting controlled by an electric field, Nat. Phys. **9**, 563 (2013).

[17] X. Xu, W. Yao, D. Xiao, and T. F. Heinz, Spin and pseudospins in layered transition metal dichalcogenides, Nat. Phys. **10**, 343 (2014).

[18] H. Zeng, J. Dai, W. Yao, D. Xiao, and X. Cui, Valley polarization in MoS$_2$ monolayers by optical pumping, Nat. Nanotechnol. **7**, 490 (2012).

[19] K. F. Mak, K. He, J. Shan, and T. F. Heinz, Control of valley polarization in monolayer MoS$_2$ by optical helicity, Nat. Nanotechnol. **7**, 494 (2012).

[20] H. Yuan, X. Wang, B. Lian, H. Zhang, X. Fang, B. Shen, G. Xu, Y. Xu, S.-C. Zhang, H. Y. Hwang *et al.*, Generation and electric control of spin–valley-coupled circular photogalvanic current in WSe$_2$, Nat. Nanotechnol. **9**, 851 (2014).

[21] O. L. Sanchez, D. Ovchinnikov, S. Misra, A. Allain, and A. Kis, Valley polarization by spin injection in a light-emitting van der Waals heterojunction, Nano Lett. **16**, 5792 (2016).

[22] Y. Ye, J. Xiao, H. Wang, Z. Ye, H. Zhu, M. Zhao, Y. Wang, J. Zhao, X. Yin, and X. Zhang, Electrical generation and control of the valley carriers in a monolayer transition metal dichalcogenide, Nat. Nanotechnol. **11**, 598 (2016).

[23] T. Norden, C. Zhao, P. Zhang, R. Sabirianov, A. Petrou, and H. Zeng, Giant valley splitting in monolayer WS$_2$ by magnetic proximity effect, Nat. Commun. **10**, 4163 (2019).

[24] S. A. Vitale, D. Nezich, J. O. Varghese, P. Kim, N. Gedik, P. Jarillo-Herrero, D. Xiao, and M. Rothschild, Valleytronics: Opportunities, challenges, and paths forward, Small **14**, 1801483 (2018).

[25] F. Langer, C. P. Schmid, S. Schlauderer, M. Gmitra, J. Fabian, P. Nagler, C. Schüller, T. Korn, P. Hawkins, J. Steiner *et al.*, Lightwave valleytronics in a monolayer of tungsten diselenide, Nature (London) **557**, 76 (2018).

[26] S. A. Oliaei Motlagh, J.-S. Wu, V. Apalkov, and M. I. Stockman, Femtosecond valley polarization and topological resonances in transition metal dichalcogenides, Phys. Rev. B **98**, 081406(R) (2018).

[27] S. A. Oliaei Motlagh, F. Nematollahi, V. Apalkov, and M. I. Stockman, Topological resonance and single-optical-cycle valley polarization in gapped graphene, Phys. Rev. B **100**, 115431 (2019).

[28] F. Nematollahi, S. A. Oliaei Motlagh, J.-S. Wu, R. Ghimire, V. Apalkov, and M. I. Stockman, Topological resonance in Weyl semimetals in a circularly polarized optical pulse, Phys. Rev. B **102**, 125413 (2020).

[29] Á. Jiménez-Galán, R. Silva, O. Smirnova, and M. Ivanov, Lightwave control of topological properties in 2D materials for sub-cycle and non-resonant valley manipulation, Nat. Photonics **14**, 728 (2020).

[30] P. Kumar, T. M. Herath, and V. Apalkov, Ultrafast valley polarization in bilayer graphene, J. Appl. Phys. **130**, 164301 (2021).

[31] M. Mrudul, Á. Jiménez-Galán, M. Ivanov, and G. Dixit, Light-induced valleytronics in pristine graphene, Optica **8**, 422 (2021).

[32] Á. Jiménez-Galán, R. E. Silva, O. Smirnova, and M. Ivanov, Sub-cycle valleytronics: Control of valley polarization using few-cycle linearly polarized pulses, Optica **8**, 277 (2021).

[33] T. Otobe, M. Yamagiwa, J.-I. Iwata, K. Yabana, T. Nakatsukasa, and G. F. Bertsch, First-principles electron dynamics simulation for optical breakdown of dielectrics under an intense laser field, Phys. Rev. B **77**, 165104 (2008).

[34] M. Noda, S. A. Sato, Y. Hirokawa, M. Uemoto, T. Takeuchi, S. Yamada, A. Yamada, Y. Shinohara, M. Yamaguchi, K. Iida *et al.*, Salmon: Scalable ab-initio light–matter simulator for optics and nanoscience, Comput. Phys. Commun. **235**, 356 (2019).

[35] Salmon official, http://salmon-tddft.jp.

[36] U. von Barth and L. Hedin, A local exchange-correlation potential for the spin polarized case. I, J. Phys. C: Solid State Phys. **5**, 1629 (1972).

[37] T. Oda, A. Pasquarello, and R. Car, Fully Unconstrained Approach to Noncollinear Magnetism: Application to Small Fe Clusters, Phys. Rev. Lett. **80**, 3622 (1998).

[38] G. Theurich and N. A. Hill, Self-consistent treatment of spin-orbit coupling in solids using relativistic fully separable *ab initio* pseudopotentials, Phys. Rev. B **64**, 073106 (2001).

[39] S. Yamada, M. Noda, K. Nobusada, and K. Yabana, Time-dependent density functional theory for interaction of ultrashort light pulse with thin materials, Phys. Rev. B **98**, 245147 (2018).

[40] S. Yamada and K. Yabana, Determining the optimum thickness for high harmonic generation from nanoscale thin films: An *ab initio* computational study, Phys. Rev. B **103**, 155426 (2021).

[41] G. F. Bertsch, J.-I. Iwata, A. Rubio, and K. Yabana, Real-space, real-time method for the dielectric function, Phys. Rev. B **62**, 7998 (2000).

[42] J. P. Perdew and Y. Wang, Accurate and simple analytic representation of the electron-gas correlation energy, Phys. Rev. B **45**, 13244 (1992).

[43] I. Morrison, D. M. Bylander, and L. Kleinman, Nonlocal Hermitian norm-conserving Vanderbilt pseudopotential, Phys. Rev. B **47**, 6728 (1993).

[44] T. C. Berkelbach, M. S. Hybertsen, and D. R. Reichman, Bright and dark singlet excitons via linear and two-photon spectroscopy in monolayer transition-metal dichalcogenides, Phys. Rev. B **92**, 085413 (2015).

[45] A. Kormányos, G. Burkard, M. Gmitra, J. Fabian, V. Zólyomi, N. D. Drummond, and V. Fal'ko, $k \cdot p$ theory for two-dimensional transition metal dichalcogenide semiconductors, 2D Mater. **2**, 022001 (2015).